Nanoscale

Accepted Manuscript

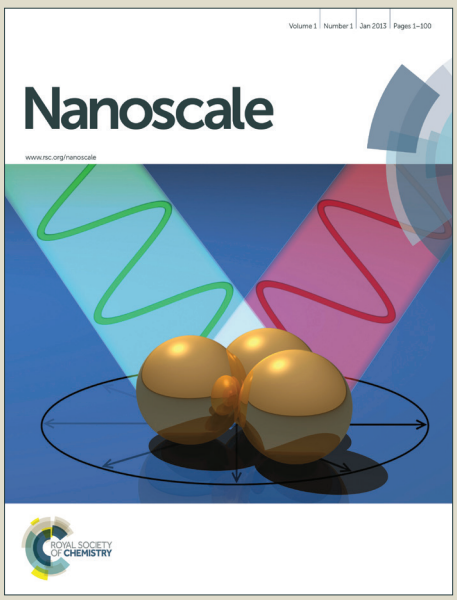

ROYAL SOCIETY OF CHEMISTRY

www.rsc.org/nanoscale

Journal Name

ARTICLE

Fast Assembling Microarrays of Superparamagnetic Fe_3O_4@Au Nanoparticle Clusters as Reproducible Substrates for Surface-Enhanced Raman Scattering

Min Ye [a], Zewen Wei [b], Fei Hu [a], Jianxin Wang[a], Guanglu Ge[b], Zhiyuan Hu[b], Mingwang Shao*[a], Shuit-Tong Lee[a] and Jian Liu*[a]

Received 00th January 20xx,
Accepted 00th January 20xx

DOI: 10.1039/x0xx00000x

www.rsc.org/

It is currently a very active research area in developing new types of substrates which integrate various nanomaterials for surface-enhanced Raman scattering (SERS) techniques. Here we report a unique approach to prepare SERS substrates with reproducible performance. It is featured with silicon mold-assisted magnetic assembling of superparamagnetic Fe_3O_4@Au nanoparticle clusters (NCs) into arrayed microstructures on a wafer scale. This approach enables the fabrication of both silicon-based and hydrogel-based substrates in a sequential manner. We have demonstrated that strong SERS signals can be harvested from these substrates due to efficient coupling effect between Fe_3O_4@Au NCs, wih enhancement factors >10^6. These substrates have been confirmed to provide reproducible SERS signals, with low variations in different locations or batches of samples. We investigate the spatial distributions of electromagnetic field enhancement around Fe_3O_4@Au NCs assemblies using finite-difference-time-domain (FDTD) simulations. The proceudre to prepare the substrates is straightforward and fast. The silicon mold can be easily cleaned out and refilled with Fe_3O_4@Au NCs assisted by a magnet, therefore being re-useable for many cycles. Our approach has integrated microarray technologies and provided a platform for thousands of independently addressable SERS detections, in order to meet the requirements of rapid, robust, and high throughput performance.

Introduction

Surface-enhanced Raman scattering (SERS) is a unique spectroscopy that offers label-free detection, high sensitivity and molecular fingerprint information. It is consequently the spectroscopy of choice in many important applications in surface physics, analytical chemistry, and pharmacology[1-4]. The occurrence of SERS hot spots on the substrate surface is often dominated by the atomic composition and local morphology on the substrate surface at the nano-scale[1, 5-7]. Varieties of nanomaterials[8, 9] have been developed for SERS applications by the introduction of fascinating heterostructures[10-17], fine-tuning hierarchical morphology on the surface[18-21], or both[22-24]. There are primarily two methods of applying these different

[a] *Institute of Functional Nano & Soft Materials (FUNSOM)*
Jiangsu Key Laboratory for Carbon-based Functional Materials & Devices
Collaborative Innovation Center of Suzhou Nano Science and Technology,
Soochow University, Suzhou, Jiangsu Province 215123, China
Email: jliu@suda.edu.cn, mwshao@suda.edu.cn
[b] *National Center for Nanoscience & Technology (NCNST)*
Chinese Academy of Science (CAS)
No.11 ZhongGuanCun BeiYiTiao, Beijing 100190, China
† M.Y. and Z.W. contribute equally to this manuscript.
Electronic Supplementary Information (ESI) available: [XRD, reflection spectra, Zeta potential, TEM images, evaluations of reproducibility, EDS, Tables of EF and RSD values of different substrates]. See DOI: 10.1039/x0xx00000x

types of nanomaterials for SERS: either in colloidal solutions[25, 26] or on the surface of solid substrates[27, 28]. The former allows for fast detection and relatively uniform SERS signals due to the stability and homogeneity of colloidal solutions, but frequently suffers from limited signal enhancement. The latter offers an opportunity to improve the detection limit, but suffers from the relatively poor performance in signal reproducibility. It remains a great challenge to develop a methodology that simultaneously enables sensitive detection, robust performance in signal reproducibility, and rapid preparation of SERS substrates.

The throughput performance is an important factor in the methodology development. As a typical high-throughput platform, the latest microarray technologies have been established by fabricating tens of thousands addressable spots in a single chip[29]. The success of the technologies in fundamental sciences and clinical medicine is largely attributed to the high-throughput performance and the ability of separately addressing each spot/probe[30, 31]. Although most of microarrays currently rely on fluorescent labeling, the great potential of SERS-based microarrays has favorably drawn the attention of scientists and researchers[32-35]. SERS-based detection has been demonstrated to be effective when the technology of protein microarrays is integrated with single-walled carbon nanotubes (SWNTs) as multicolor Raman tags. It has achieved the sensitivity nearly three orders of magnitude better than standard fluorescence assays[32]. In addition, microarrays of gold nanoparticles clusters have been proposed by the method of discontinuous (so-called Stop & Go) convective self-assembly, and evaluated for SERS signal quality as patterned substrates (2×3 arrays)[35]. Continuous convective self-assembly has also been employed to produce topologically patterned substrates containing gold or silver nanoparticles on the two-dimensional surface[36]. Patterned arrays of microstructures containing in situ-grown Ag nanoparticles have been fabricated on mesoporous silica films as SERS devices by a synchrotron-based approach[37]. However, there is still plenty of room for improvement in SERS-based microarrays in terms of throughput or signal reproducibility.

Here we report our new efforts in addressing this challenge by the development a robust approach to prepare microarrays of superparamagnetic Fe_3O_4@Au nanoparticle clusters (NCs) as SERS substrates. This approach is featured with silicon mold-assisted magnetic assembly of composite nanoparticle clusters on a wafer scale. It can produce both silicon-based and hydrogel-based substrates in a sequential manner. These substrates include a great number of arrayed microstructures on their surface, either micro-wells (silicon-based) or micropillars (hydrogel-based) which integrated dense aggregates of Fe_3O_4@Au NCs. We have demonstrated that both the silicon-based and hydrogel-based substrates can produce strong SERS signals with minimal variations from different locations of a substrate or between different batches of samples. We have applied finite-difference-time-domain (FDTD) simulations to calculate the distributions of electromagnetic-field enhancement around Fe_3O_4@Au NCs assembled by our approach. Although magnetic separation has widely been used in previous reports, it is mainly to pre-concentrate the analytes from the diluted solutions onto hybrid nanomaterials, which turns out to be effective in improving the detection limit[38, 39]. In a comparison of excluding the pre-concentration effect, the EF values of our substrates are close to those similar types of hybrid nanomaterials with high performance[38, 39]. However, our work is an important research progress in the aspects of large-scale integration of individually addressable SERS detections and robust performance. It has provided a unique approach to transfer nanoparticles from the colloidal solution to the solid surface and assemble them into arrayed microstructures rapidly for SERS detection. This work represents the first methodological demonstration of SERS microarrays using both silicon-based and hydrogel-based substrates with highly reproducible signals.

Results and discussion

As shown in Figure 1, our unique approach enables fabricating two types of substrates contain microarrays of Fe_3O_4@Au NCs in a sequential manner, included silicon-based and hydrogel-based substrates. Briefly, an ethanol suspension of Fe_3O_4@Au NCs was dripped onto the silicon mold, which had been positioned on the top of a magnet. Therefore, superparamagnetic Fe_3O_4@Au NCs quickly precipitated into the bottom of micro-wells due to the attraction of the magnet underneath. This setup was held for a few minutes till the ethanol evaporated. This procedure of dripping, magnetic assisted precipitation, and solvent evaporation was repeated for several times. It facilitated the formation of dense aggregates of Fe_3O_4@Au NCs, due to the synergistic effect of attraction by the magnet, evaporation of solvent, and the physical confinement by the walls of silicon micro-wells. Afterwards, adhesive tape was used to remove any scattered Fe_3O_4@Au NCs outside the micro-wells, leaving the silicon mold with a clean surface. These steps produced a silicon-based substrate containing microarrays of Fe_3O_4@Au NCs ready for SERS experiments, which also allowed subsequent processing to prepare a hydrogel-based substrate. A pre-gel solution containing acrylamide monomers (AAm), crosslinker, initiator and cofactor molecules was added on the surface of the silicon-based substrate[40, 41]. After the mixture solution solidified, peeling off the layer of polyacrylamide (PAM) hydrogel can replicate the arrayed microstructures of the silicon mold. Therefore the well-confined aggregates of Fe_3O_4@Au NCs were successfully transferred from the silicon mold onto the surface of the PAM hydrogel microstructures, forming a hydrogel-based substrate.

Superparamagnetic Fe_3O_4@Au nanoparticle clusters were synthesized by a layer-by-layer assembling approach[42]. The surface of Fe_3O_4 nanoparticle was modified by dopamine (DA) molecules *via* complexation of iron ions and phenolic hydroxyl groups, thus becoming hydrophilic and positively-charged[43]. Gold seeds were adsorbed and assembled on the surface of Fe_3O_4-DA nanoparticles through the electrostatic interactions, and further aged in an Au growth solution[42]. This procedure created Fe_3O_4 nanoparticles enclosed by a dense layer of

protruding Au antenna nanostructures. This morphology was typically favored in active SERS substrates. The intermediate products during the synthesis procedure, including Fe_3O_4 nanoparticles without or with Au seeds, and clusters of Fe_3O_4@Au nanoparticle clusters, were characterized by transmission electron microscopy (TEM) (Figure 2a-c). The diameter of Fe_3O_4 nanoparticles was approximately 106 nm. The feature size of Au antenna nanostructures on the surface was nearly 16 nm. Energy-dispersive X-ray mapping was employed to analyze the presence and distribution of iron (Fe), oxygen (O) and gold (Au) elements in Fe_3O_4@Au (Figure 2d). The crystallinity of the Fe_3O_4 nanoparticles and Fe_3O_4@Au NCs was investigated by high-resolution TEM (HRTEM) (Figure 2e and f, respectively). As for Fe_3O_4 nanoparticles, the lattice spacings of two adjacent planes were 0.48 nm and 0.24 nm, corresponding to the (111) and (22-2) planes of cubic magnetite (Figure 2e). As for Fe_3O_4@Au NCs, the lattice spacing of 0.23 nm was corresponding to the (111) planes of the face-centered cubic (FCC) Au crystallite (Figure 2f). X-ray diffraction (XRD) measurements further confirmed the high degree of crystallinity in the Fe_3O_4 nanoparticles and Fe_3O_4@Au NCs (ESI Figure S1a). The characteristic surface plasmon resonance (SPR) absorption of Au nanostructures around 520 nm was successfully detected in the reflection spectra of the aqueous solutions of Fe_3O_4@Au NCs (ESI Figure S1b). Zeta potential measurements of the intermediate products also revealed distinct changes in their surface properties, which was consistent to our expectation based on the assembling strategy by electrostatic interactions (ESI Figure S2).

Both the samples of Fe_3O_4 nanoparticles and Fe_3O_4@Au NCs quickly responded to the external magnetic field in a reversible manner. When an external magnetic field was applied to an aqueous solution containing either Fe_3O_4 nanoparticles or Fe_3O_4@Au NCs, they can rapidly be attracted by the magnet. When the magnet was removed away, they became well dispersed again in the solution without aggregation (Figure 2g, inset). Magnetic hysteresis measurements revealed that the magnetization of the samples shortly became saturated and exhibited zero remanence or coercive force. It provided a good demonstration of the superparamagnetic property with our samples, which allowed for fast assembling in response to an external magnetic field, without the side effect of remanence. Previously, a weakening effect was reported for the SERS signals when Au nanoparticles were assembled with magnetic microspheres and then exposed to an external magnetic field[44]. However, our experiments adopted a different approach to avoid the undesired weakening effect: on one hand, superparamagnetic Fe_3O_4 nanoparticles were utilized in this work to eliminate magnetic remanence, instead of magnetic microspheres; on the other hand, the external magnetic field was removed during SERS measurements.

A silicon mold containing arrays of micro-wells was fabricated with standard MEMS (Micro-electro-mechanical system) processes, including dicing, lithography and dry etching. As shown in Figure 3a-c, arrays of micro-wells were etched on the silicon wafer. In total, more than 1.4×10^5 micro-wells were etched in a piece of 4 inch wafer. Detailed information including the feature size, spacing, and arrangement of micro-wells is available in the experimental section. The silicon-based substrate containing microarrays of Fe_3O_4@Au NCs was imaged by SEM (Figure 3d-f). The micro-wells of the silicon mold were filled with Fe_3O_4@Au NCs, in comparison with the control of an empty mold (Figure 3a-c). The fillings of Fe_3O_4@Au were confined by the boundary of each micro-well, so that the spots on the microarrays were uniform overall. Any residues outside the micro-wells were cleaned to help reduce undesired background noise in SERS detection. We also imaged the aggregation status of Fe_3O_4@Au NCs and observed a distinctive difference when they were deposited with or without an external magnetic field (ESI Figure S3a-b).

The silicon-based substrates containing microarrays of Fe_3O_4@Au NCs were examined for SERS signals of R6G molecules (a standard analyte due to its well-established characteristics of molecular vibrations). The R6G solutions were added on the surface of the silicon-based substrates. Individual micro-wells on the substrates from different batches were measured for SERS signals. We detected the characteristic Raman peaks of R6G of high intensity including those at 1312, 1363, 1510, and 1650 cm^{-1} (Figure 4a). These peaks derived from molecular vibrations of R6G carbon skeleton in the stretching modes[45]. These measurements suggested an efficient coupling effect between individual Fe_3O_4@Au NCs in the micro-wells for signal amplification. Different concentrations of R6G solutions were tested using the silicon-based substrates, ranging from 10^{-5} M to 10^{-7} M. The results demonstrated good correlation between the SERS intensity and the concentration of R6G molecules. The SERS enhancement factors (EF) of the silicon-based substrates were further evaluated with the equation[46] of $EF=I_{SERS}N_0/I_0N_{SERS}=I_{SERS}C_0/I_0C_{SERS}$. The values of Raman intensity at the specific wave number (I_{SERS}) in the specified concentration (C_{SERS}) of R6G were measured from the spectra using our SERS substrates, while I_0 was measured from solid R6G on a blank silicon mold of micro-wells without fillings. Different types control substrates were prepared, including type 1: Fe_3O_4@Au NCs deposited into the micro-wells of the mold without a magnet; type 2: Fe_3O_4@Au NCs deposited onto the smooth wafer with a magnet; type 3: Fe_3O_4@Au NCs deposited onto the smooth wafer without a magnet; and type 4: a monolayer of Fe_3O_4@Au NCs directly deposited on a smooth wafer without an external magnetic field. The SERS enhancement factors of the silicon-based substrates were around 7×10^6, nearly two or three orders of magnitude higher than the controls (ESI Table 1). These calculations supported that our approach of silicon mold-assisted magnetic assembly provided a higher SERS coupling with Fe_3O_4@Au NCs than the other types of controls.

We further demonstrated that the silicon-based substrates produced SERS signals with an excellent uniformity within individual micro-wells, between different micro-wells, or between different batches of substrates. The SERS signals of

R6G molecules were detected by sampling the inner surface of individual micro-wells. As shown in Figure 4b, the Raman spectra of R6G from different locations of the micro-wells included the characteristic peaks of R6G molecules. The profiles of these peaks were highly reproducible, which indicated nearly homogeneous distribution and stacking of Fe_3O_4@Au NCs within the micro-wells. We also verified low signal variations among different micro-wells or separate batches of samples. Separate batches including repeated sample substrates (12 in total) were examined in identical conditions for SERS signals (Figure 4c and ESI Figure S4). Statistical analysis was performed on the intensities of the characteristic peaks measured at different micro-wells of each silicon-based substrate. As shown in Figure S4, each column represented the averaged intensity of the Raman peak at the specified wavenumber from different micro-wells, with an error bar of standard deviation (SD) showing the well-to-well variations (n=5) of individual substrates. The values of relative standard deviation (RSD) of the columns were mostly smaller than 20%, indicating that the substrates were sufficient uniform for practical SERS applications[47]. Then the intensities from 12 separate sample substrates were averaged, with error bars (SD) showing the sample-to-sample variations of different batches (n=12, Figure 4c). The RSD values for the Raman peaks at 1312, 1363, 1510 and 1650 cm^{-1} were 13.7%, 14.7%, 13.2%, and 13.0%, respectively (Figure 4c). Therefore the results of analysis supported that our approach can produce reliable SERS signals with practically minimum spatial variations, compared with other types of control substrates (ESI Table 2). Furthermore, we established that our silicon-based substrates can be recycled[38, 48], according to a fill-clean-refill protocol. As shown in Figure 4d, we adopted ultrasonication to remove the fillings of Fe_3O_4@Au NCs and clean the silicon mold after we completed the first round of SERS measurements. Then we refilled the same silicon mold with Fe_3O_4@Au NCs by following the same steps outlined previously. We measured the SERS signals for the second round from the same set of micro-wells (n=5) with new fillings because each micro-well was addressable. This protocol was repeated for 5 cycles in our demonstration. In each cycle the averaged intensities of characteristic Raman peaks were plotted as the dots arranged in the vertical column, with error bars (SD) showing well-to-well variations (Figure 4d). No signal was detected when the fillings of Fe_3O_4@Au NCs was cleaned out the micro-wells of the silicon mold. Consistent SERS signals were measured after refilling of the silicon mold in all the cycles, which evidenced the robustness and reproducibility of our assembly method.

We created hydrogel-based substrates containing microarrays of Fe_3O_4@Au NCs with the technique of soft lithography. In our approach, the pre-gel solution containing acrylamide monomers (AAm) and cofactor molecules was spread on the surface of the silicon-based substrates with Fe_3O_4@Au NCs fillings till its solidification. The process time to prepare the PAM hydrogel-based substrates was controlled to approximately 1 hour to allow for good molding to the substrates. The hydrogel-based substrates now contained arrayed micropillars, the reverse of the micro-wells from the silicon mold. Aggregates of Fe_3O_4@Au NCs were immobilized by the sol-gel transition and transferred into the top of individual micropillars. As shown in the optical micrographs, arrays of PAM hydrogel micropillars were prepared from a blank silicon mold (Figure 5a) and the silicon-based substrates containing Fe_3O_4@Au NCs (Figure 5b-c). The features of the micro-wells including sizes and shapes can be replicated in well-defined details to the micropillar structures. The PAM hydrogel surface around the micropillars was clean, suggesting no undesired residues left by the procedure. A zoomed-in view of the micropillar top revealed that aggregates of Fe_3O_4@Au NCs were transferred and distributed in the hydrogel with good homogeneity (Figure 5c). SEM images and the EDS analysis of the hydrogel-based substrates also confirmed the transfer and nearly uniform layout of Fe_3O_4@Au NCs from the micro-wells to the micropillars (ESI Figure S5). SERS signals of R6G in different concentrations were detected with the PAM hydrogel-based substrates, exhibiting the characteristic peaks including 1312, 1363, 1510, and 1650 cm^{-1}(Figure 5d-f and ESI Table 1, EFs $\sim 10^6$). We performed multiple rounds of experiments and confirmed that the hydrogel-based substrates can produce SERS signals with excellent reproducibility within the individual micropillars, between micropillars, and from batch to batch (Figure 5e, f and ESI Table 2). PAM hydrogel has been widely used in electrophoresis for the separation of biomolecules including nucleic acids or proteins. Aggregates of Fe_3O_4@Au NCs are embedded inside the top layer of PAM hydrogel with our approach. This geometry is different from the other conventional two-dimensional SERS substrates using silicon wafer. Therefore, our hydrogel-based approach may offer to detect biomolecules with SERS in situ after nucleic acids or proteins of different molecular weight are separated in the PAM hydrogel by electrophoresis.

In order to investigate the coupling effect between Fe_3O_4@Au NCs for SERS amplification, a well-established simulation method using finite-difference-time-domain (FDTD) was employed to calculate the distributions of EM-field enhancement[49]. We built a model of packing the balls of different sizes to mimic the aggregated Fe_3O_4@Au NCs by the silicon mold-assisted magnetic assembly. The parameters including the diameters of particles, distances or gaps were mainly referred to the statistical measurements using TEM images. For instance, the diameter of a single Fe_3O_4@Au NC was 138 nm, including the core of Fe_3O_4 (106 nm) and a layer of small Au balls (16 nm). There were 130 gold balls symmetrically assembled on the surface of each Fe_3O_4 core. Fe_3O_4@Au NCs were arranged at the vertices of a square lattice. The gap distance including 1 nm, 2 nm, or 6 nm between adjacent Fe_3O_4@Au NCs was empirically chosen and tested in order to simulate their aggregated status by the external magnetic field. Additionally, simulation was also performed for an isolated Fe_3O_4@Au NC to mimic the aggregation-free status without magnetic assembling. In the simulation, the electromagnetic wave of laser propagated from top to bottom in the x-z plane with planar polarization in the x direction and perpendicular to the x-y plane (Figure 6a).

The intensities of electric field of Fe_3O_4@Au NC in these two different conditions were monitored and compared by FDTD in a z-scan manner. As shown in Figure 6b&c and Figure S7, there were mainly two regions where the electric field in the x-y plane was significantly enhanced, resulting from the aggregated status by magnetic assemblies. The enhancement of electric field in Region I was dominated by the contribution of intra-particle (Au balls) within individual Fe_3O_4@Au NC. In contrast, the effect in Region II was dominated by the contribution of inter-particle (Au balls) from two adjacent but different Fe_3O_4@Au NCs. Interestingly, in region II the contribution of intra-particle (Au balls) within the same Fe_3O_4@Au NC provided only a little to the enhancement of the electric field. These highly localized features in coupling were representative for the layers of gold balls (z=0 nm, z=18.5 nm, or z=-18.5 nm), but became weak in other layers of gold balls in the z-scan. In contrast, for an isolated Fe_3O_4@Au NC (aggregation-free), there was little enhancement of electric field by the coupling of gold balls (Figure 6d-e). These simulation results suggested a critical role of the aggregation status of Fe_3O_4@Au NC in amplifying SERS signals. These simulations provided valuable support for our observation of significant SERS enhancement in our substrates, but also provided interesting details regarding the spatial distribution of the coupling effect of Au in the Fe_3O_4@Au nanoparticle clusters.

Experimental

Materials

Acrylamide (AAm) and ammonium persulfate (APS) were purchased from TCI and Amresco, respectively. N,N,N′,N′-Tetramethylethylenediamine (TEMED), N,N′-methylene bis(acrylamide) (MBA), tetrakis (hydroxymethyl) phosphonium chloride (THPC) solution, dopamine (DA), Rhodamine 6G were obtained from Sigma-Aldrich. $HAuCl_4 \cdot 4H_2O$, ferric chloride hexahydrate ($FeCl_3 \cdot 6H_2O$), sodium acetate (NaOAc), ethanol, ethylene glycol (EG), diethylene glycol (DEG), tetrahydrofuran (THF), acetic acid, potassium carbonate (K_2CO_3), formaldehyde were obtained from Sinopharm Chemical Reagent. The RbFeB magnets (3800 Gs) were purchased from the Link Company (Beijing).

Preparation of Fe_3O_4 nanoparticles modified with dopamine

$FeCl_3 \cdot 6H_2O$ (1.08 g) and NaOAc (4 g) were dissolved in EG (14 mL) and DEG (26 mL) with rapid magnetic stirring till the solution turned an earthy yellow. The solution was transferred into three Teflon-lined stainless-steel autoclaves (20 mL in volume), sealed and heated at 200℃ in an oven for 15 h. After the autoclave was cooled to room temperature, Fe_3O_4 nanoparticles were washed with water and ethanol twice respectively, and then dried under vacuum for 12 h. Fe_3O_4 NPs (20 mg) were re-suspended in 5 mL THF. An aqueous solution of dopamine (1% w/w) was added into the suspension and sonicated for 1 h. Then the solution was put onto a shaking table for thorough mixing overnight at room temperature. The Fe_3O_4-DA nanoparticles were finally purified by magnetic separation and then re-dispersed in 20 mL water.

Synthesis of Fe_3O_4@Au nanoparticle clusters

Gold seeds were prepared by adding 2 mL $HAuCl_4$ (1%) into a solution premixed with 12 µL THPC (80% v/v), 0.25 mL NaOH (2 M), and 45 mL deionized water. The mixture was stirred overnight in dark conditions. The solution of gold seeds (8 mL) was added into 5 mL Fe_3O_4-DA (1 mg/mL) aqueous solution, so that the negative charged gold seeds could be assembled onto the surface of positively charged Fe_3O_4-DA by an electrostatic interaction. Acetic acid (0.2 M) was introduced to adjust the pH value of the solution to 4. The mixture was shocked vigorously overnight. Magnetic separation was employed to remove the excess gold seeds. Then the intermediate product was mixed with the Au growth solution ($HAuCl_4$ 0.015% w/w, K_2CO_3 0.025% w/w) under vigorous stirring. Formaldehyde (29% v/v) was introduced to the mixture as the reducing agent in drops. The final product of Fe_3O_4@Au nanoparticle clusters was purified by magnetic separation and re-dispersed in ethanol before use.

Fabrication of the silicon molds containing arrays of micro-wells

The mold was fabricated with standard MEMS (Micro-electro-mechanical system) processes, including dicing, lithography and dry etching. Briefly, a thin aluminum layer (300 nm) was sputtered on a 4-inch n-type silicon wafer with (100) orientation (LuoYang Single Crystal Silicon Co., China). UV Photolithography was used to pattern a 2 µm thick RZJ304 photoresist (Ruihong Fine Chemistry, China) layer to the mask for aluminum etching. After removing the residual photoresist by nitrosonitric acid, the aluminum layer was patterned by the potassium hydrate solution. Using the patterned aluminum layer as the mask, the micro-well array was formed by the ICP (Inductively Coupled Plasma) etching. Finally, the aluminum layer was removed and the silicon wafer was diced with proper size to form the micro-mold. A piece of 4 inch wafer was used to prepare 30 identical unit pieces (1.8 cm × 1 cm). Each unit piece contained six types of micro-wells with different diameters, including 25, 50, 75, 100, 125 and 150 µm, arranged in sub-arrays (4681 micro-wells in each unit). The spacing between two neighboring wells was 100 µm. The depth of the wells was 8 µm approximately. There were more than 1.4×10^5 micro-wells in total in a single piece of 4 inch wafer.

Fabrication of the silicon-based substrates

The surface of the silicon mold was cleaned with oxygen plasma treatment (1 min). It was put on top of a RbFeB magnet. An ethanol solution of Fe_3O_4@Au NCs was added onto the silicon mold. Fe_3O_4@Au NCs were pulled down by the magnet and fill the micro-wells of the silicon mold. The ethanol solvent was evaporated in a few minutes. The procedure of filling and solvent evaporation was repeated twice more on the silicon mold. Adhesive tapes were used to remove the excess materials outside the micro-wells. After this process, the silicon-based substrates containing arrays of micro-wells were ready for SERS measurements.

Fabrication of the hydrogel-based substrates

A protocol of preparing the pre-gel solution of polyacryamide (PAM) was followed with a few home-made modifications. In brief, 3.17 mL AAm monomer (20% w/w) and 1.21 mL MBA (1% w/w) pre-

dissolved in a DPBS buffer were mixed. Then 1.5 μL TEMED and 47 μL APS (10% w/w in DPBS buffer) were added into the solution and mixed thoroughly. The solution was transferred onto the silicon-based substrate with the RbFeB magnet underneath. The pre-gel solution solidified completely in 1 h. The layer of PAM hydrogel containing arrays of micropillars was peeled off from the silicon mold, ready for SERS measurements as hydrogel-based substrates.

Characterization facilities

Scanning Electron Microscope (SEM) and Transmission Electron Microscope (TEM) images were obtained using Quanta 200 FEG and Tecnai F20 (FEI, USA) respectively. X-Ray Powder Diffraction (XRD) was performed in Cu tubes using an Empyrean (Netherlands PANalyticle). Measurements of ultraviolet and visible spectrophotometer (UV-Vis) were performed with Lambda 750 (Perkin Elmer). Raman spectra in the SERS measurements were acquired using a Laser confocal microscopy Raman spectrometer (Lab RAM HR 800, France Jobin Yvon). The magnetic hysteresis curves were obtained using a physical property measurement system (PPMS-9, Quantum Design, USA). Zeta potential measurements were performed with a Zetasizer Nano ZS (ZEN3690, Malvern). Optical micrographs were obtained using the microscope (DM4000M, Laica). A software package of finite-difference-time-domain (FDTD) (Lumerical Solutions, Inc., Vancouver, Canada) was used for simulations of the electromagnetic field enhancement.

Measurements of SERS signals

Raman spectroscope (LabRAMHR 800, Jobin Yvon) equipped with a synapse CCD detector was used to detect SERS signals of R6G molecules on different types of substrates including the silicon-based or hydrogel-based ones. A He-Ne laser of 633 nm (10 mW) was used for excitation. SERS spectra were collected at 50× objective (numerical aperture 0.90, Olympus) from 1000 cm^{-1} to 1800 cm^{-1}. The accumulation time was set as 1 second and identical for all the SERS measurements. The silicon-based substrates were tested by dripping different concentrations of R6G solutions on the surface. The hydrogel-based substrates were tested by immersing them in different concentration of R6G. Separate SERS measurements were performed from at least 5 different locations (including micro-wells or micropillars) for each sample substrate. Different batches of substrates (in total 12 separate samples for silicon-based substrates, 10 separate samples for hydrogel-based substrates) were tested for validation of reproducibility.

Simulation with the finite-difference-time-domain (FDTD) method

Simulations were performed with the software package of FDTD Solutions from Lumerical solutions, Inc. (Vancouver, Canada). An individual Fe_3O_4@Au NC was 138 nm in diameter and symmetrically encompassed with 130 gold balls (16 nm in diameter). In order to shorten the simulation time, a simplified square lattice was used to mimic the aggregates of Fe_3O_4@Au NCs by putting an individual NC at vertices with the edge-to-edge gap distance of 1, 2, or 6 nm. The results with the gap distance of 6 nm were shown in Figure 6. The results with the gap distance of 1 nm and 2 nm were shown in the ESI (Figure S7). An isolated Fe_3O_4@Au NC was also simulated to mimic the aggregation-free status without magnetically assisted assembling. The plane wave of a laser (633 nm) was placed above the Fe_3O_4@Au NCs with polarization along the x-axis. The experimental value of Palik 27 was used for the dielectric constant of Au. The mesh size was set as 1 nm × 1 nm × 1 nm in the calculations. The simulation time was set at 500 fs, ensuring enough time for the fields to decay completely before termination of the simulation. To obtain the electric field distribution around the Fe_3O_4@Au NPs, frequency-domain field profile monitors (x-z and y-z plane) were placed layer-by-layer through the nanoparticle cluster to record the electromagnetic field over the simulation region. The electric field intensity distribution was reported as the square of the electric field ($|E/E_0|^2$).

Conclusions

In summary, we have developed a robust approach to prepare silicon-based and hydrogel-based substrates containing a large number of addressable microstructured arrays for SERS applications. Our approach enables a rapid transfer (3-5 s) of Fe_3O_4@Au NCs from the colloidal solution to the inner surface of micro-wells arrayed on the silicon mold with the external magnetic field. Interestingly, the fillings of Fe_3O_4@Au NCs can be transferred again from the silicon mold onto the PAM hydrogel micropillars with the technique of soft lithography. We have demonstrated that strong SERS signals can be harvested from these silicon-based or hydrogel-based substrates. Our findings imply that an efficient coupling effect between Fe_3O_4@Au NCs occurs in our assemblies. Our substrates have been confirmed to provide reproducible signals in SERS measurements, with low variations in different locations or batches of samples. FDTD simulations have promoted our understanding on spatial distribution of EM-field enhancement around Fe_3O_4@Au NCs assemblies. Our substrates can be prepared in straightforward and fast manner (silicon-based in 10 min; hydrogel-based in 1 h). The silicon-based substrates can be easily cleaned out and refilled with Fe_3O_4@Au NCs assisted by a magnet, therefore being re-useable for many cycles. The arrayed microstructures on the substrates are individually addressable, allowing for detection of multiple different samples in parallel in a single chip. Therefore, our approach offers a flexible platform for SERS applications requiring high throughput performance and sufficient robustness, for example, in rapid detection of pesticide residues or in monitoring food safety[4, 33, 50, 51].

Acknowledgements

This work was supported by the Major State Basic Research Development Program (2013CB932702, 2012CB932601), and by the National Natural Science Foundation of China (21275106); a project supported by the Priority Academic Program Development of Jiangsu Higher Education Institutions, and a Doctoral Fund of Ministry of Education of China (20123201120025). J.L. was supported by the "Youth 1000-plan" in the Recruitment Program of Global Experts. We thank Dr. John Mcleod for his helpful discussion and suggestions in revising the manuscript. M.Y. and Z.W. contribute equally to this manuscript.

Notes and references

1. A. Campion and P. Kambhampati, *Chem. Soc. Rev.*, 1998, **27**,241-250.
2. S. Nie and S. R. Emory, *Science*, 1997, **275**, 1102-1106.
3. K. Kneipp, Y. Wang, H. Kneipp, L. T. Perelman, I. Itzkan, R. R. Dasari and M. S. Feld, *Phys. Rev. Lett.*, 1997, **78**, 1667-1670.
4. J. F. Li, Y. F. Huang, Y. Ding, Z. L. Yang, S. B. Li, X. S. Zhou, F. R. Fan, W. Zhang, Z. Y. Zhou, Y. WuDe, B. Ren, Z. L. Wang and Z. Q. Tian, *Nature*, 2010, **464**, 392-395.
5. S. Lal, N. K. Grady, J. Kundu, C. S. Levin, J. B. Lassiter and N. J. Halas, *Chem. Soc. Rev.*, 2008, **37**, 898-911.
6. K. A. Willets, *Chem. Soc. Rev.*, 2014, **43**, 3854-3864.
7. H. Wei and H. Xu, *Materials Today*, 2014, **17**, 372-380.
8. M. J. Banholzer, J. E. Millstone, L. Qin and C. A. Mirkin, *Chem. Soc. Rev.*, 2008, **37**, 885-897.
9. Y. Xiong, J. M. McLellan, J. Chen, Y. Yin, Z. Y. Li and Y. Xia, *J. Am. Chem. Soc.*, 2005, **127**, 17118-17127.
10. Z. Xu, Y. Hou and S. Sun, *J. Am. Chem. Soc.*, 2007, **129**, 8698-8699.
11. A. Musumeci, D. Gosztola, T. Schiller, N. M. Dimitrijevic, V. Mujica, D. Martin and T. Rajh, *J. Am. Chem. Soc.*, 2009, **131**, 6040-6041.
12. C. Cheng, B. Yan, S. M. Wong, X. Li, W. Zhou, T. Yu, Z. Shen, H. Yu and H. J. Fan, *ACS Appl. Mater. Interfaces*, 2010, **2**, 1824-1828.
13. Z. Huang, G. Meng, Q. Huang, Y. Yang, C. Zhu and C. Tang, *Adv. Mater.*, 2010, **22**, 4136-4139.
14. X. Chen, S. Li, C. Xue, M. J. Banholzer, G. C. Schatz and C. A. Mirkin, *ACS Nano*, 2009, **3**, 87-92.
15. Q. An, P. Zhang, J.-M. Li, W.-F. Ma, J. Guo, J. Hu and C.-C. Wang, *Nanoscale*, 2012, **4**, 5210-5216.
16. X. Ding, L. Kong, J. Wang, F. Fang, D. Li and J. Liu, *ACS Appl. Mater. Interfaces*, 2013, **5**, 7072-7078.
17. J. Shen, Y. Zhu, X. Yang, J. Zong and C. Li, *Langmuir*, 2013, **29**, 690-695.
18. R. n. A. Alvarez-Puebla, A. Agarwal, P. Manna, B. P. Khanal, P. Aldeanueva-Potel, E. Carbó-Argibay, N. Pazos-Péreza, L. Vigderman, E. R. Zubarev, N. A. Kotov and L. M. Liz-Marzán, *Proc. Nat. Acad. Sci.*, 2011, **108**, 8157-8161.
19. A. Gopalakrishnan, M. Chirumamilla, F. De Angelis, A. Toma, R. P. Zaccaria and R. Krahne, *ACS Nano*, 2014, **8**, 7986-7994.
20. K. Jung, J. Hahn, S. In, Y. Bae, H. Lee, P. V. Pikhitsa, K. Ahn, K. Ha, J.-K. Lee, N. Park and M. Choi, *Adv. Mater.*, 2014, **26**, 5924-5929.
21. L. Jiang, Y. Tang, C. Liow, J. Wu, Y. Sun, Y. Jiang, Z. Dong, S. Li, V. P. Dravid and X. Chen, *Small*, 2013, **9**, 705-710.
22. J. P. Lee, D. Chen, X. Li, S. Yoo, L. A. Bottomley, M. A. El-Sayed, S. Park and M. Liu, *Nanoscale*, 2013, **5**, 11620-11624.
23. L.-F. Zhang, S.-L. Zhong and A.-W. Xu, *Angew. Chem. Int. Ed.*, 2013, **52**, 645-649.
24. D. Liu, X. Wang, D. He, T. D. Dao, T. Nagao, Q. Weng, D. Tang, W. Tian, D. Golberg and Y. Bando, *Small*, 2014, **10**, 2564-2569.
25. X. Qian, X. Zhou and S. Nie, *J. Am. Chem. Soc.*, 2008, **130**, 14934-14935.
26. M. Hardy, M. D. Doherty, I. Krstev, K. Maier, T. Moller, G. Muller and P. Dawson, *Anal. Chem.*, 2014, **86**, 9006-9012.
27. R. F. Aroca, P. J. Goulet, D. S. dos Santos, Jr., R. A. Alvarez-Puebla and O. N. Oliveira, Jr., *Anal. Chem.*, 2005, **77**, 378-382.
28. C. Tian, C. Ding, S. Liu, S. Yang, X. Song, B. Ding, Z. Li and J. Fang, *ACS Nano*, 2011, **5**, 9442-9449.
29. H. Sun, G. Y. Chen and S. Q. Yao, *Chem. Biol.*, 2013, **20**, 685-699.
30. M. Schena, D. Shalon, R. W. Davis and P. O. Brown, *Science*, 1995, **270**, 467-470.
31. P. Tissari, A. Zumla, E. Tarkka, S. Mero, L. Savolainen, M. Vaara, A. Aittakorpi, S. Laakso, M. Lindfors, H. Piiparinen, M. Maki, C. Carder, J. Huggett and V. Gant, *Lancet*, 2010, **375**, 224-230.
32. Z. Chen, S. M. Tabakman, A. P. Goodwin, M. G. Kattah, D. Daranciang, X. Wang, G. Zhang, X. Li, Z. Liu, P. J. Utz, K. Jiang, S. Fan and H. Dai, *Nat. Biotech.*, 2008, **26**, 1285-1292.
33. D. Qi, L. Lu, L. Wang and J. Zhang, *J. Am. Chem. Soc.*, 2014, **136**, 9886-9889.
34. M. C. Wu, Y. Chou, C. M. Chuang, C. P. Hsu, J. F. Lin, Y. F. Chen and W. F. Su, *ACS Appl. Mater. Interfaces*, 2009, **1**, 2484-2490.
35. C. Farcau, N. M. Sangeetha, N. Decorde, S. Astilean and L. Ressier, *Nanoscale*, 2012, **4**, 7870-7877.
36. V. Liberman, C. Yilmaz, T. M. Bloomstein, S. Somu, Y. Echegoyen, A. Busnaina, S. G. Cann, K. E. Krohn, M. F. Marchant and M. Rothschild, *Adv. Mater.*, 2010, **22**, 4298-4302.
37. L. Malfatti, P. Falcaro, B. Marmiroli, H. Amenitsch, M. Piccinini, A. Falqui and P. Innocenzi, *Nanoscale*, 2011, **3**, 3760-3766.
38. X. Zhang, Y. Zhu, X. Yang, Y. Zhou, Y. Yao and C. Li, *Nanoscale*, 2014, **6**, 5971-5979.
39. X. X. Han, A. M. Schmidt, G. Marten, A. Fischer, I. M. Weidinger and P. Hildebrandt, *ACS Nano*, 2013, **7**, 3212-3220.
40. J. Hu, C. Liu, L. Chen, W. Xing and J. Luan, *Exp. Ther. Med.*, 2014, **7**, 681-684.
41. T. Vignaud, H. Ennomani and M. Thery, *Methods. Cell. Biol.*, 2014, **120**, 93-116.
42. Z. Li, S. Yin, L. Cheng, K. Yang, Y. Li and Z. Liu, *Adv. Funct. Mater.*, 2014, **24**, 2312-2321.
43. M. D. Shultz, J. U. Reveles, S. N. Khanna and E. E. Carpenter, *J. Am. Chem. Soc.*, 2007, **129**, 2482-2487.
44. X. Kong, Q. Chen, R. Li, K. Cheng, N. Yan and B. Yu, *Chem. Commun.*, 2011, **47**, 11237-11239.
45. J. A. Dieringer, K. L. Wustholz, D. J. Masiello, J. P. Camden, S. L. Kleinman, G. C. Schatz and R. P. Van Duyne, *J. Am. Chem. Soc.*, 2008, **131**, 849-854.
46. K. Kim, H. S. Han, I. Choi, C. Lee, S. Hong, S.-H. Suh, L. P. Lee and T. Kang, *Nat. Commun.*, 2013, **4**.
47. M. J. Natan, *Faraday Discussions*, 2006, **132**, 321-328.
48. X. Yang, H. Zhong, Y. Zhu, J. Shen and C. Li, *Dalton transactions*, 2013, **42**, 14324-14330.
49. J. Ye, F. Wen, H. Sobhani, J. B. Lassiter, P. Van Dorpe, P. Nordlander and N. J. Halas, *Nano Lett.*, 2012, **12**, 1660-1667.
50. A. P. Craig, A. S. Franca and J. Irudayaraj, *Annu. Rev. Food. Sci. Technol.*, 2013, **4**, 369-380.

51. X. Liu, C. Zong, K. Ai, W. He and L. Lu, *ACS Appl. Mater. Interfaces*, 2012, **4**, 6599-6608.

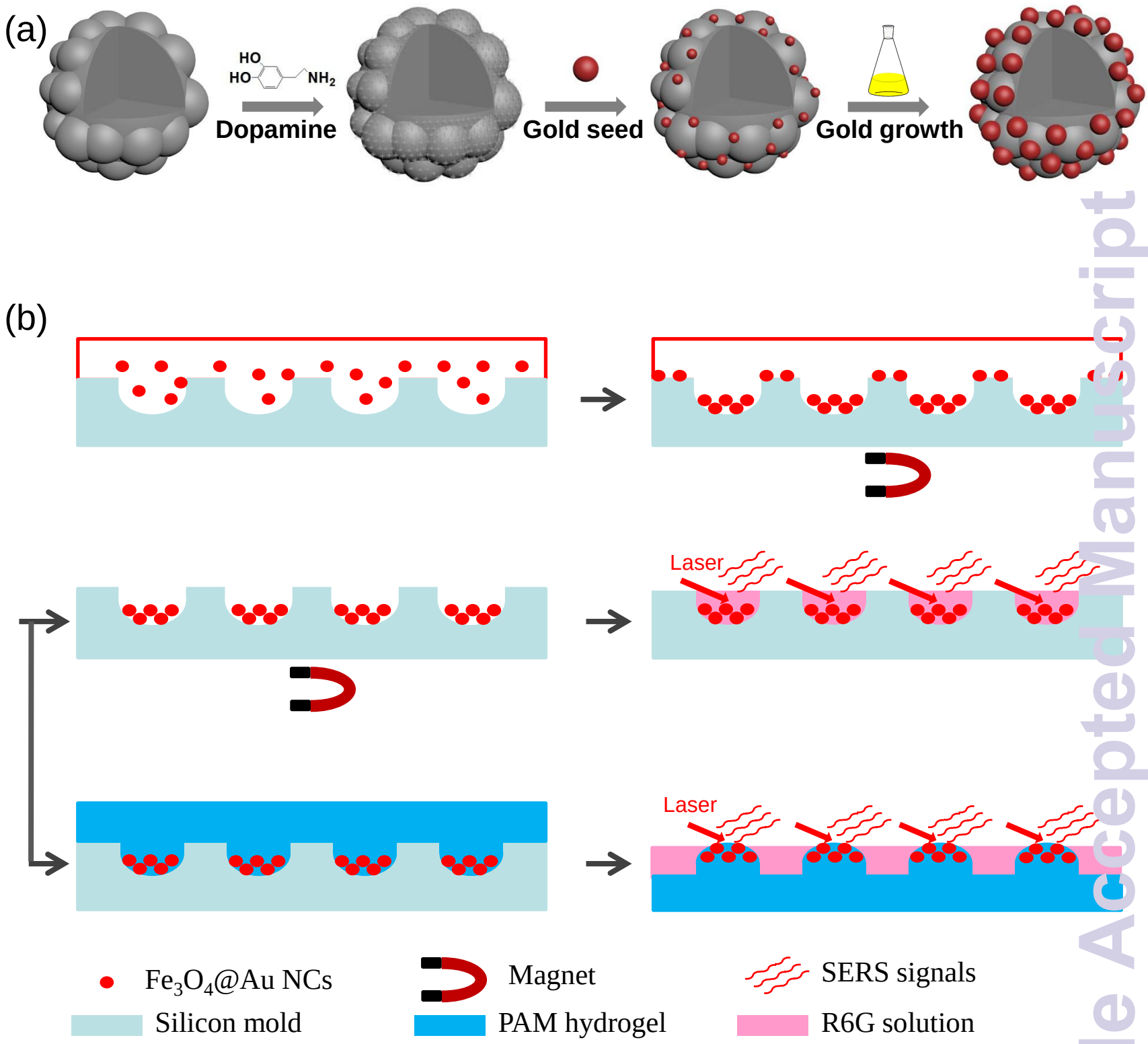

Figure 1. a) The synthesis procedure of the Fe_3O_4@Au NCs by a layer-by-layer assembling approach. b) Schematic illustration of preparing the silicon-based and hydrogel-based substrates for SERS in a sequential manner.

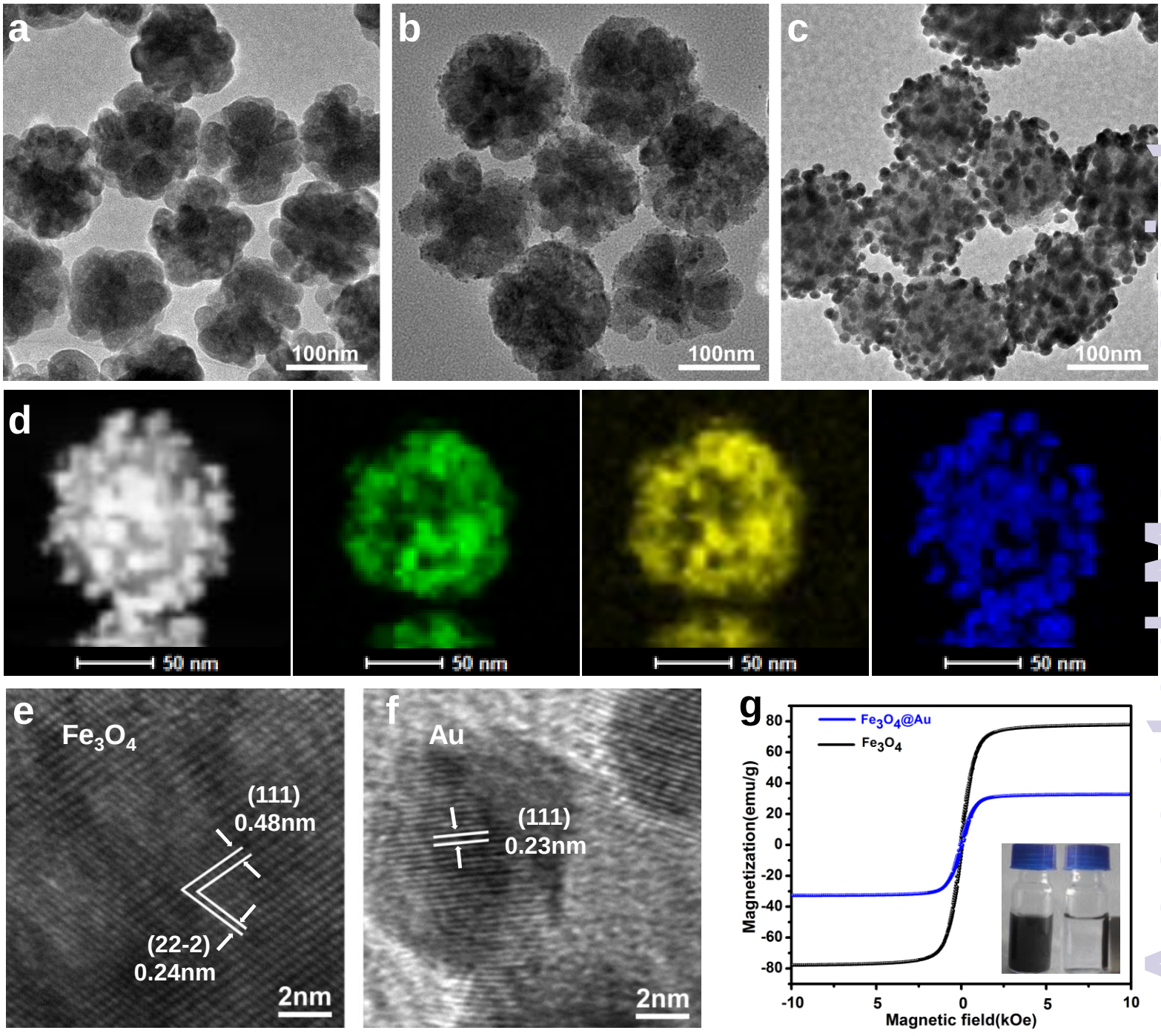

Figure 2. Characterization of Fe_3O_4@Au NCs. a-c) TEM images of Fe_3O_4 NPs, Fe_3O_4 NPs absorbed with gold seeds, and Fe_3O_4@Au NCs, respectively. d) Scanning transmission electron microscopy (STEM) images of Fe_3O_4@Au NCs. Elements of Fe (green), O (yellow) and Au (blue). e-f) HRTEM images of Fe_3O_4 NPs and Fe_3O_4@Au NCs, respectively. g) The magnetic hysteresis curves of Fe_3O_4 NPs and Fe_3O_4@Au NCs. Inset: an optical micrograph of Fe_3O_4@Au NCs aqueous solution without (left) and with (right) exposure to an external magnetic field.

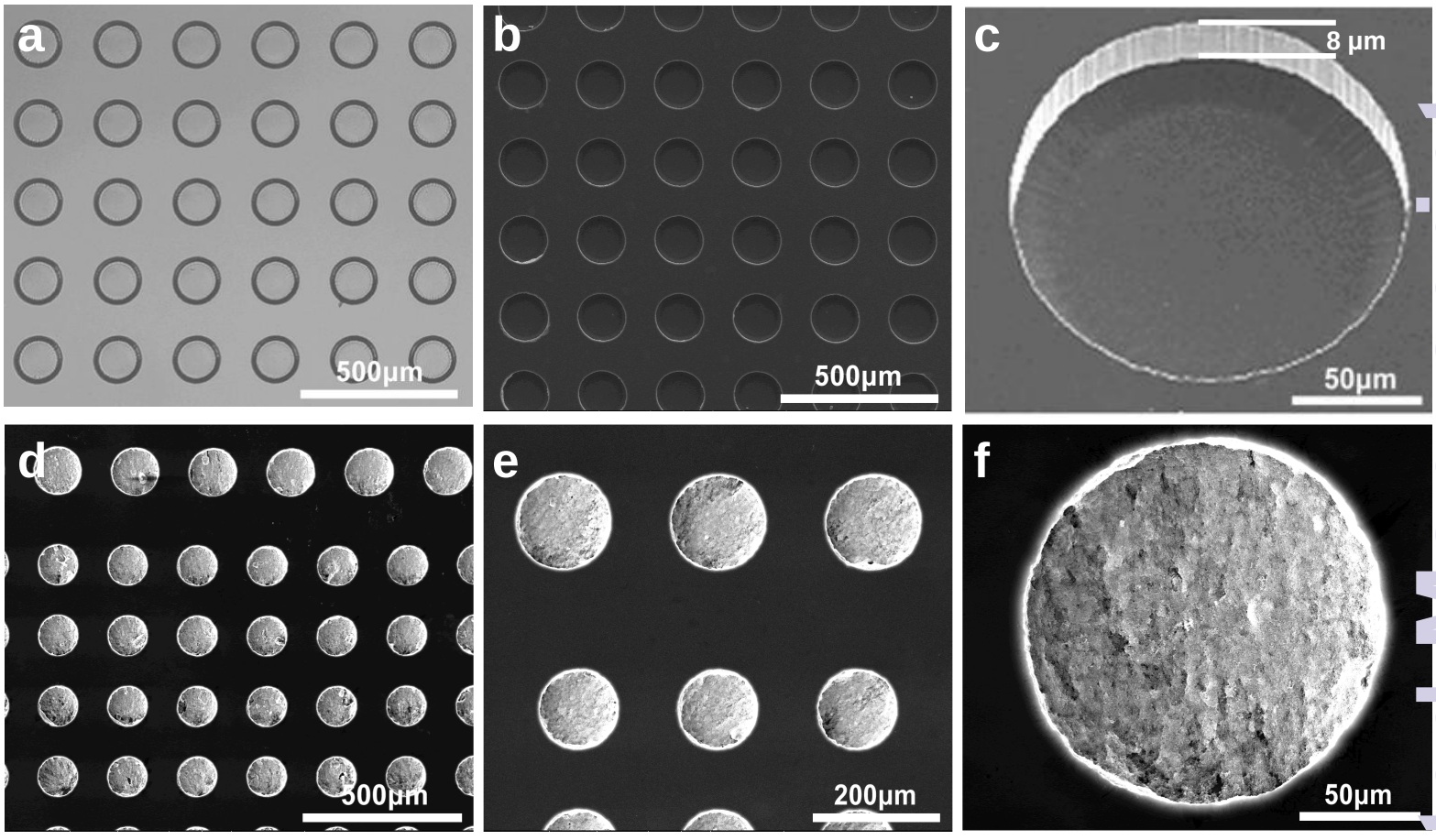

Figure 3. a) Optical micrograph, b-c) SEM images of the silicon mold. d-f) SEM images of the silicon-based substrate with Fe_3O_4@Au NCs filled in the micro-wells. The panels of d) and e) show sub-arrays of micro-wells with different diameters.

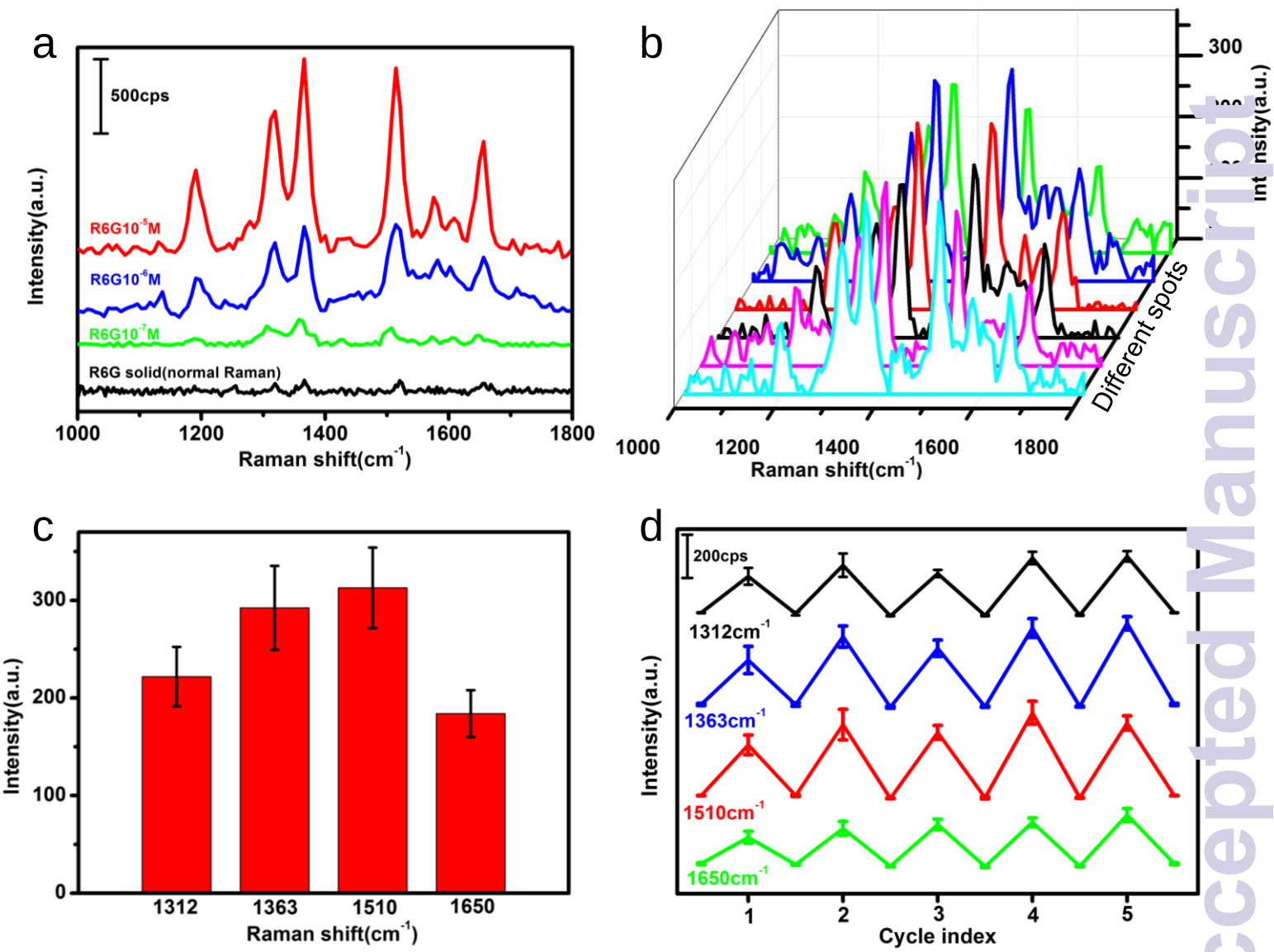

Figure 4. a) SERS signals of 10^{-5}, 10^{-6} and 10^{-7} M Rhodamine 6G (R6G) enhanced by the silicon-based substrates, black curve: normal Raman in the blank control. b) Reproducible SERS signal profiles from the different locations of the inner surface of one micro-well, R6G (1×10^{-6} M). c) Reproducibility of SERS signals showing sample-to-sample variations in different batches of the silicon-based substrates, error bar: standard deviation of different samples (n=12), R6G (1×10^{-6} M). d) Evaluation of reusability of the silicon-based substrate by the fill-clean-refill protocol for five cycles, error bar: standard deviation of different micro-wells (n=5), R6G (1×10^{-6} M).

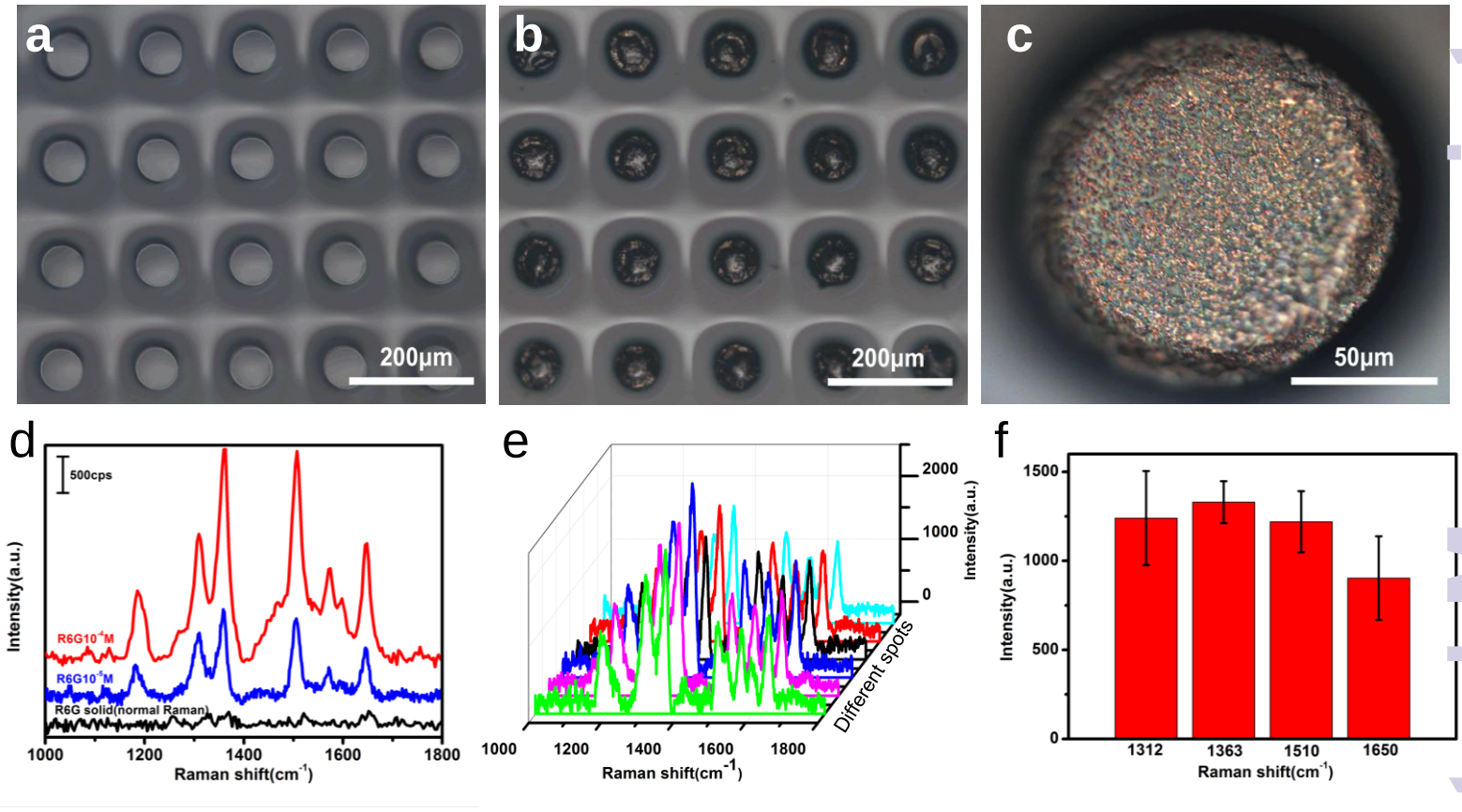

Figure 5. a) Optical micrograph of the PAM hydrogel replicate from a blank silicon mold without Fe_3O_4@Au NC fillings. b-c) Optical micrographs of the hydrogel-based substrate with aggregation of Fe_3O_4@Au NCs transferred into the top of PAM hydrogel micropillars. d) SERS signals of R6G (10^{-4} M and 10^{-5} M) enhanced by PAM hydrogel-based substrate, black curve: normal Raman in the blank control. e) Reproducible SERS signal profiles from the different locations of one PAM hydrogel micropillar, R6G (1×10^{-5} M). f) Reproducibility of SERS signals showing sample-to-sample variations in different batches of the PAM hydrogel-based substrates, error bar: standard deviation of different samples (n=10), R6G (1×10^{-5} M).

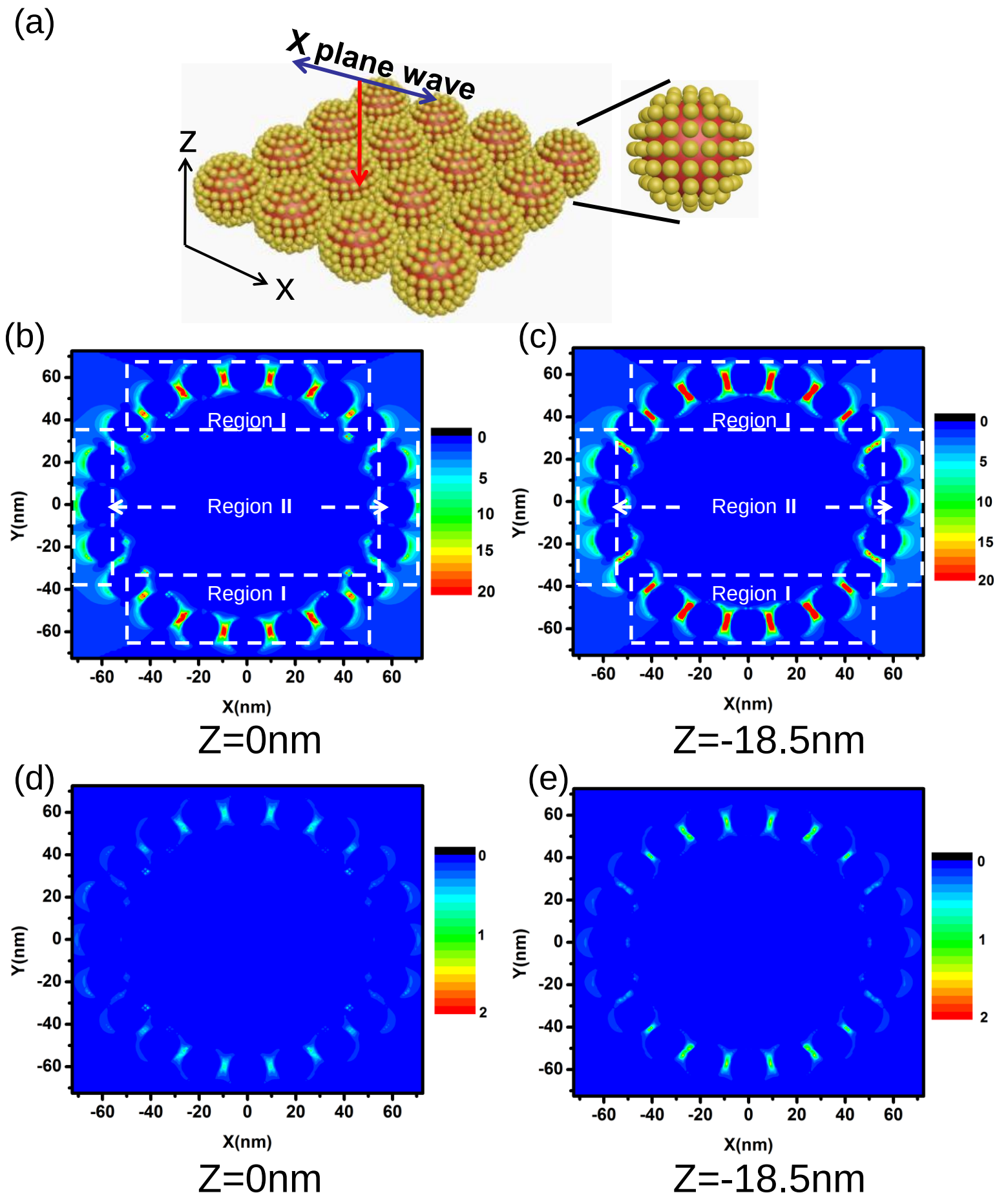

Figure 6. a) Schematic illustration of the Fe_3O_4@Au NCs model in the FDTD simulations, drawing not according to the exact scale. b-c) Simulated electromagnetic field distribution of the Fe_3O_4@Au NC at the x-y plane of z=0 nm and z=-18.5 nm in the aggregated status, respectively. Gap distance between NCs: 6 nm. d-e) Simulated electromagnetic field distribution of an isolated Fe_3O_4@Au NC (aggregation-free) at the x-y plane of z=0 nm and z=-18.5 nm, respectively.